Acta Oceanol. Sin., 2015, Vol. 34, No. 7, P. 1–18
DOI: 10.1007/s13131-015-0693-1
http://www.hyxb.org.cn
E-mail: hyxbe@263.net

Comparative simulation study of effects of eddy-topography interaction in the East/Japan Sea deep circulation

CHOI Youngjin[1, 2*]

[1] Center for Earth Information Science and Technology, Japan Agency for Marine-Earth Science and Technology, Yokohama 236-0001, Japan

[2] GeoSystem Research Corporation, Gyeonggi-do 435-824, Korea

Received 27 May 2014; accepted 10 October 2014

Abstract

In this study the structure and seasonal variations of deep mean circulation in the East/Japan Sea (EJS) were numerically simulated using a mid-resolution ocean general circulation model with two different parameterizations for the eddy-topography interaction (ETI). The strong deep mean circulations observed in the EJS are well reproduced when using the ETI parameterizations. The seasonal variability in the EJS deep layer is shown by using ETI parameterization based on the potential vorticity approach, while it is not shown in the statistical dynamical parameterization. The driving mechanism of the strong deep mean currents in the EJS are discussed by investigating the effects of model grids and parameterizations. The deep mean circulation is more closely related to the baroclinic process and potential vorticity than it is to the wind driven circulation.

Key words: East/Japan Sea, deep mean current, seasonal variability, ocean general circulation model, eddy-topography interaction

Citation: CHOI Youngjin. 2015. Comparative simulation study of effects of eddy-topography interaction in the East/Japan Sea deep circulation. Acta Oceanologica Sinica, 34(7): 1–18, doi: 10.1007/s13131-015-0693-1

1 Introduction

In recent years it has become evident that the Japan/East Sea (hereafter EJS) deep circulation has a horizontal cyclonic structure and seasonal variability whereby deep currents are activated in the early spring season (Senjyu et al., 2005; Takematsu et al., 1999). Choi and Yoon (2010, henceforth CY10) studied the strong deep mean currents by observational analysis using moored current meter data and autonomous float trajectories. They showed that the deep mean currents generally follow the ambient potential vorticity (f/H), and suggested a detailed structure of deep mean circulation in the EJS. The temporally and spatially averaged deep mean current is approximately 2.8 cm/s and the volume transport in the EJS deep layer (deeper than 800 m) is more than 10×10^6 m^3/s. Strong seasonal variations of approximately 30% of the mean velocity were also observed. The present study designed numerical simulations for investigating strong deep mean currents in the EJS, with special emphasis on the parameterization of eddy-topography interaction (ETI).

Many numerical analysis papers have discussed the deep circulation in the EJS. Sakai and Yoshikawa (2005) conducted a simple two-layer model experiment with a simple rectangular basin to understand the mechanisms generating the deep mean flow in the EJS through ETI. Hogan and Hurlburt (2000) showed eddy-driven deep mean flows in the EJS using the Naval Research Laboratory's Layered Ocean Model (NLOM) with extremely fine horizontal grid intervals ($\leqslant (1/64)°$) and four vertical levels. They suggested that a horizontal grid interval of at least $(1/32)°$ is required to reproduce the cyclonic deep mean flow without parameterization of the subgrid-scale eddies. They showed that the deep mean current in the EJS follows the f/H contours of the bottom topography. Kim (2007) also obtained a cyclonic deep mean current using a primitive ocean general circulation model (OGCM) with extra-fine resolution (a horizontal grid interval of $(1/36)°$ and 46 vertical levels), although its amplitude is much less than the observed 2–6 cm/s (Mori et al., 2005). Therefore, eddy-resolving OGCM results with an extra-fine resolution support the idea that the cyclonic flows in the EJS deep layer are eddy-driven, because previous numerical simulations with a coarse or medium resolution ($(1/6)°$ to $(1/12)°$) grid did not reproduce such strong cyclonic deep circulation in the EJS (Kim and Yoon, 1996; Seung and Yoon, 1995; Yoon and Kawamura, 2002). However, the extra fine resolution in a primitive OGCM, such as that used by Kim (2007), requires excessive amounts of computational and economic resources.

An alternative modeling approach to reduce the costs and computer time required is to parameterize subgrid-scale eddies so as to reproduce eddy effects on the mean flow even in models with coarse resolutions. From the early 1990s, many studies have parameterized the effects of mesoscale eddies in coarse resolution ocean models. Holloway (1992) proposed the "Neptune effect" (hereafter NE), which parameterizes the stress resulting from ETI. By statistical dynamical analysis in an ideal quasi-geostrophic system, Salmon et al. (1976) showed that an ocean with no external forcing and filled with random eddies will tend to set up a mean flow directed as found in topographic Rossby wave propagation.

Holloway (1992) suggested the reproduction of ETI in numerical ocean models, with a tendency of the system towards a

Foundation item: The Research Program on Climate Change Adaptation (RECCA) of the Ministry of Education, Culture, Sports, Science and Technology (MEXT) of Japan.

*Corresponding author, E-mail: himrchoi@gmail.com

defined equilibrium state, based on the work by Salmon et al. (1976). The statistical subgrid scale tendency driven by the ETI is thought to occur due to the difference between the instantaneous velocity field and the velocity field of the ocean's defined equilibrium state. An estimate of the force generated by the ETI effect is 0.1–1 N/m^2 (Holloway, 1992), which is as large as or even larger than the typical wind stresses thought to be a dominant driving mechanism for the ocean. By including the topostress in a coarse resolution OGCM ((1/4)°), Holloway et al. (1995) were successful in reproducing a strong cyclonic deep mean circulation in the EJS.

Although the NE is effective, NE parameterization has limitations. It assumes an eddy-driven flow as a steady state, but deep flows in the real ocean are never in a steady state. Moreover, barotropic forcing generated by the NE governs circulations throughout the water column, while flows in the EJS deep layer show quasi-barotropic features (Kitani, 1987; Takematsu et al., 1999).

Greatbatch (1998), and Greatbatch and Li (2000) (hereafter GL) proposed a new parameterization for the form drag working along the isopycnal surface, following ideas of Gent and McWilliams (1990) (hereafter GM90). The difference is that GL incorporate the stress from the bottom topography, whereas GM90 neglect the bottom stress.

Our purpose in this study is to describe how well the deep mean circulation and the seasonal variability of the EJS deep layer are simulated when using an OGCM with appropriate parameterizations. This paper is organized as follows. Section 2 describes the features of an ocean model and parameterizations. The results of numerical experiments are then presented and compared with observations in Section 3. Summary and discussion are presented in Section 4.

2 Japan/East Sea ocean model and observational data

2.1 *General setup of a numerical model*

The ocean model used in this study was developed at the Research Institute for Applied Mechanics (RIAM) at Kyushu University (Lee et al., 2003) and is called as RIAMOM (RIAM Ocean Model). The RIAMOM is a three-dimensional z-coordinate ocean circulation model with hydrostatic and Boussinesq approximations and an Arakawa B-grid (Mesinger and Arakawa, 1976). Free-surface primitive equations are solved in the model. The RIAMOM implements a momentum advection scheme that allows slant advection at the lateral boundary (Ishizaki and Motoi, 1999). This model also uses an improved tracer advection scheme called the modified split quadratic upstream interpolation for convective kinetics scheme (MSQUICK; Webb et al., 1998). For the upper ocean mixed layer, it also incorporates the scheme proposed by Noh (1996).

The topography is extracted from the world digital elevation model ETOPO5 (NCAR, 1989) for deeper regions (below 500 m) and from Sungkyunkwan University (SKKU) 1 min data manually digitized from the marine chart (Choi et al., 2002) for shallower regions (upper 500 m). A maximum depth of 3 640 m is assumed in the simulations. The model covers the entire EJS from 33° to 52°N latitude longitude and from 126.5° to 142.5°E (Fig. 1). The horizontal grid interval is (1/6)° in both latitudinal and longitudinal directions. The number of vertical levels is 46 and the vertical grid intervals vary from a minimum of 15 m at the surface to a maximum of 200 m at the deepest grid.

The values of all constants used in the model are given in Table 1. In a finite difference formulation in OGCM, A_H should be chosen sufficiently large to prevent a false computational space oscillation from appearing in the numerical solution (Takano, 1974). The numerical value for A_H is based on convergence tests made by Wallcraft et al. (2005). The coefficient of harmonic horizontal and vertical eddy viscosity, A_H and A_V are assumed to be constant; the value of A_H=1.0×10^6 cm^2/s has been used in the simulations, and the same value for horizontal diffusivity. For the vertical eddy viscosity A_V, 1.0 cm^2/s is adopted following previous EJS model study performed by Seung and Yoon (1995).

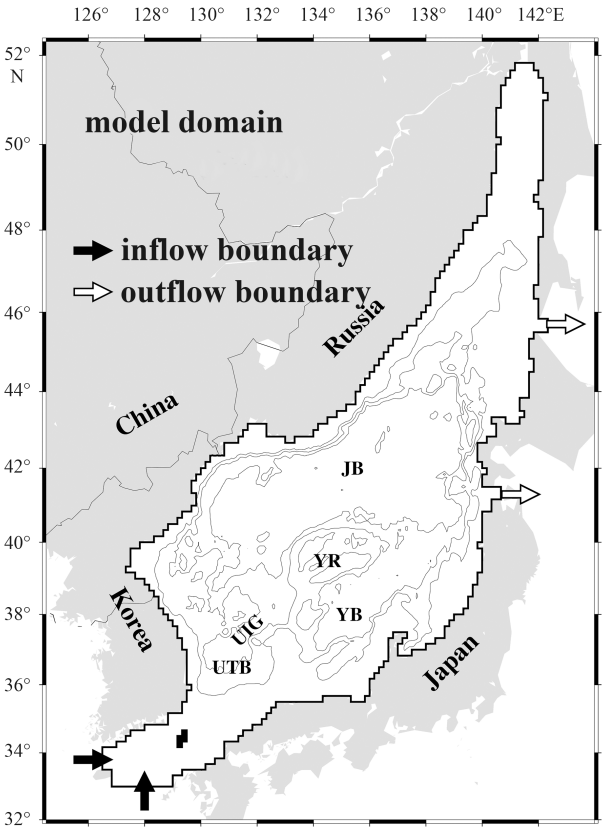

Fig. 1. Model domain and topography of (1/6)° resolution. Contours indicate bottom topography with 1 000 m interval. Black and white arrows indicate inflow and outflow boundary, respectively.

The model has two inflows in the Tsushima/Korea (T/K) Straits. One is the Jeju Strait and the other is the cross-section parallel to the latitude line connecting the southern part of Jeju Island to the west coast of Kyushu. There are also two outflows, the Tsugaru Strait and Soya Strait (Fig. 1). The monthly volume transports through the T/K Straits is taken from Takikawa and Yoon (2005). The outflows through the Tsugaru and Soya Straits are assigned 65% and 35% of the inflow transport, respectively.

The wind stress fields used in this study are taken from the European Centre for Medium-Range Weather Forecasts (ECMWF) operational forecast model output with a resolution of 0.562 5° for the period between 1992 and 1999. The model sea surface temperature and sea surface salinity are restored to monthly averaged climatology values using a Newtonian restoring time of five days. The sea surface temperature was provided by Minobe et al. (2004) who used an optimal interpolation tech-

nique to reproduce a seawater temperature dataset of the EJS' upper 400 m from 1930 to 1996. Climatological monthly averages from 1987 to 1996 were used. Since the influence of salinity variation is greater at lower temperatures, this study used a Russian sea surface salinity dataset, provided by Luchin et al. (2003), rather than Japanese or Korean data.

Table 1. Model experiments and parameters setup

CASE		A_H/cm^2·s^{-1}	A_V/cm^2·s^{-1}	Time step	L/km	κ/cm^2·s^{-1}
NE	NE1				5	–
	NE2				6	–
	NE3				7	–
		1.0×10^6	1.0	40 s		
GL	GL1				–	1×10^5
	GL2				–	2×10^5
	GL3				–	3×10^5

2.2 *Parameterizations of the roles of mesoscale eddies in mean flow*

This study adopts first the parameterization suggested by Holloway (1992). His idea is that ETIs generate entropy, which makes a system tend towards an equilibrium (maximum entropy) state.

Holloway (1992) defines a stream function representing an equilibrium state as $\psi^* = -fL^2H$, where H is the bottom topography, f is the Coriolis parameter, and L is a scale factor. Then, the horizontal velocity u is replaced by $u-u^*$ in the horizontal viscosity term, $A_H\nabla_h^2(\boldsymbol{u}-\boldsymbol{u}^*)$, where u^* is obtained from the stream function ψ^* such that the horizontal velocity u is restored to an equilibrium velocity u^*.

Holloway (1992) also suggested that L corresponds to a length scale characterizing eddy vorticity, and numerical experiments using quasi-geostrophic models appear consistent with this identification (Eby and Holloway, 1994; Holloway et al., 1995). L is usually given a simple value in marginal seas. In practice, Holloway et al. (1995) prescribed L to vary from 4 to 6 km in the coarse resolution EJS model. This study tests three cases wherein each case has a constant L from 5 to 7 km (Table 1).

Greatbatch (1998) and GL suggested an ETI parameterization in terms of a potential vorticity approach. Mesoscale eddies induce pressure variations as well as height variations along isopycnal surfaces. The covariance of pressure and height acts as a stress acting on an isopycal surface. GL named the stress due to mesoscale eddies as eddy stress—a kind of form drag working on an isopycnal surface. They parameterized eddy stress following the idea of GM90. GL is distinguished from GM90, in which stress is neglected by incorporating the form drag (stress) from the bottom topography against the water lying over it. The details of the GL parameterization are described in Appendix.

2.3 *Numerical model experiment setup*

Numerical model experiments are conducted for three cases: without parameterization (WP), with the NE, and the parameterization of GL. To examine the most appropriate empirical parameter, the NE and GL cases are run using three different scenarios, respectively (Table 1). Each case is integrated over 30 years from an initial state at rest. The last one-year data is used for analysis.

The simulated results are vertically averaged from 800 m to bottom to investigate the mean flow field in the EJS deep layer, under the approximation that the EJS deep layer under 800 m is quasi-homogeneous and ventilation from surface and intermediated water is negligibly small (Senjyu and Sudo, 1996; Takematsu et al., 1999).

2.4 *Observational data*

In order to evaluate reproducibility of simulation results, this study referred Lagrangian trajectories and Eulerian long-term direct current measurements which had been conducted in the EJS deep layers. Both data were handled and provided by Choi and Yoon (2010). During 1999–2006 the deep circulation is surveyed by 38 PALACE floats of the Office of Naval Research (ONR) Japan/East Sea project (Danchenkov et al., 2003) and 27 APEX floats of Meteorological Research Institute (METRI) under the ARGO project. 4 632 displacement velocities were obtained from the float trajectories at parking depth of 800×10^3 Pa, then the irregularly distributed displacements are re-gridded onto regularly spaced grids of (1/6)°×(1/6)° (provided in Fig. 11d for comparison with simulations). An average value at a regularly spaced grid point is calculated by nearest-neighborhood method (Wessel and Smith, 1998). The Eulerian long-term direct current measurements were conducted in the deep basins of the EJS between 1993 and 2003. The descriptions on the mooring data are listed in Table 2. Random uncertainty and tides were removed by a 3-sigma quality control method and 24-h tide killer filter (Hanawa and Mitsudera, 1985), respectively.

3 Results

3.1 *Effects of horizontal grid interval on model results*

This study first evaluate the effect of horizontal resolution by comparing our model results with the extra-fine resolution ((1/36)°) model results by Kim (2007) (hereafter EF). Figure 2 shows correlations between the annually averaged model velocities and the velocities obtained by moored current meters. The correlation between the WP and current meter velocities is almost zero. The correlation between the EF and current meter velocities slightly increases to 0.16. The magnitude of the velocity in the EF model results increases, with a magnitude of the mean velocity approximately 1.5 times larger than in the WP case. The maximum velocity in the WP is only 1.75 cm/s, whereas that in the EF is 3.79 cm/s. Differences in the current direction between the model and the observed velocities are also shown (Fig. 3). The averaged difference in current direction in the WP case is approximately 1.4 times larger than in the EF model results.

Annually averaged deep mean current velocity fields (at depths of 1 000, 2 000 and 3 000 m) for EF are shown in Fig. 4. Two major features are found in EF's deep mean current fields. First, the deep mean currents basically follow the f/H contours, as seen in Fig. 5. Second, the current structure at each depth is strongly coherent, suggesting that the deep mean circulation in the EJS is barotropic or quasi-barotropic. These features corres-

Table 2. Summary of current meter data. Each column indicates: observation name (mooring), mooring site (site), north latitude (lat), west longitude (lon), current meter depth (depth), and observation periods (from start time (start) to end time (end)), respectively

Mooring	Site	Lat/(°)	Lon/(°)	Depth/m	Start	End
Khromov	M1	43.72	137.91	1 000/2 000/2 500	Aug. 1993	Jun. 2001
	M2	40.69	136.24	1 000/2 000/2 600	Aug. 1993	Jun. 2001
	M3	41.33	134.36	1 000/2 000/3 000	Aug. 1993	Aug. 1996
	M4	41.30	132.40	1 300/2 100/2 900	Jul. 1994	Aug. 1995
	M5	39.63	132.42	900/1 900/2 400	Jul. 1994	Aug. 1996
	M6	42.42	133.56	800/1 800/2 400	Aug. 1995	Jun. 2003
	MK	41.00	133.50	1 000/3 000	Jul. 2000	Jul. 2001
	MS	41.25	132.20	1 700/2 500/3 200	May 1999	Jul. 2001
	P1	40.11	133.32	1 000/3 000	Aug. 2000	Jul. 2002
	P2	40.50	134.99	1 000/2 500	Aug. 2000	Jul. 2002
	PS	41.24	132.34	1 000/2 800	Jul. 2000	Jul. 2001
Kakuyo	A3	36.38	134.92	400/600/700	May 1995	May 1997
	B2	37.43	135.66	1 000/2 500	Jun. 1999	Jun. 2000
	B4	37.99	135.04	1 000/2 000	Jun. 1999	Jun. 2000
	C5	37.34	133.64	1 000/1 400	Jun. 1999	Jun. 2000
	C9	38.65	133.66	900/2 000	Jun. 1998	Jun. 2000
	D6	36.35	132.13	1 000/1 400	Jun. 1998	Jun. 2001
	E5	38.33	136.50	1 000/2 000	Jun. 2002	Jun. 2003
	G4	37.54	132.32	1 500	Jun. 2002	Jun. 2003
	K6	37.99	135.04	1 000/2 000	Jun. 2002	Jun. 2003
	K7	37.35	133.64	1 000/1 500	Jun. 2001	Jun. 2002
	Y	37.43	135.66	1 000/2 500	Jun. 2000	Jun. 2001
	Y1	37.64	134.79	800/1 800/2 800	Jun. 1997	Jun. 1998
	Y2	37.66	135.36	700/1 800/2 800	Jun. 1997	Jun. 1998
	Y3	38.04	135.06	800/1 900/2 800	Jun. 1997	Jun. 1998
	Y4	37.41	135.66	1 700	Jun. 1998	Jun. 1999
Melville	R1	37.72	129.62	1 200	Jun. 1999	Jun. 2001
	R2	37.75	129.95	1 600	Jun. 1999	Apr. 2001
	R3	37.66	130.40	1 600	Jun. 1999	Jul. 2001
	R4	37.72	132.20	2 500	Jun. 1999	Jun. 2001
	R5	37.47	129.96	1 500	Jun. 1999	Jul. 2001
	R6	37.24	130.67	2 200	Jul. 1999	Jun. 2001
	R7	36.86	130.05	2 200	Jun. 1999	Jul. 2001
	R9	36.13	130.15	1 500	Jun. 1999	Jun. 2001
	RN	36.28	131.50	1 800	Jun. 1999	Jun. 2001
	RS	36.12	131.50	1 500	Jun. 1999	Jun. 2001
Oshoro	IS	40.61	139.36	300/2 100	Apr. 1994	Apr. 1995
Hokusui	HU	42.50	139.17	400/700/2 200	Jun. 1998	Jun. 1999

pond well with the observed features shown in past studies (Hirose et al., 2007; Takematsu et al., 1999; CY10).

3.2 *Empirical parameter tests*

Three model experiment cases are conducted to find the most appropriate empirical parameters in the NE and GL runs (Table 1). As addressed in Holloway et al. (1995), the empirical parameters for ETI makes up errors in forcing and is dependent upon model resolution and parameters. Therefore the parameter L should have different values in each model. Comparisons of velocity magnitudes in each case, as well as mooring observations, are shown in Figs 6 (NE) and 7 (GL), respectively. Among the NE cases, NE3 shows the highest correlation (0.77) between the model and the mooring observations, as compared with NE1 (0.61) and NE2 (0.72). In the GL experiments, the GL2 correlation (0.80) is higher than the others (0.70 for GL1 and 0.78 for GL3).

The differences in the current direction between the simulated and the observed velocities are shown in Figs 8 (NE) and 9 (GL), respectively. The angular differences in the NE3 and GL1 cases are 26.13° and 16.68°, respectively, which represent the smallest differences among each series of the experiment. On the other hand, the empirical parameters L (NE) and κ (GL) primarily influence the magnitude of the current velocity. In both cases, variations in the current direction differences among the cases are quite small compared with variations in the differences in magnitude. Therefore, this study adopts magnitude as the main criteria and selects the NE3 and GL2 cases for analysis. Hence-

forth, NE3 and GL2 are referred to as NE and GL, respectively. Note that the parameter L of 6 km is the upper value of the range suggested by Holloway et al. (1995) (L is 4 to 6 km) for the EJS simulation.

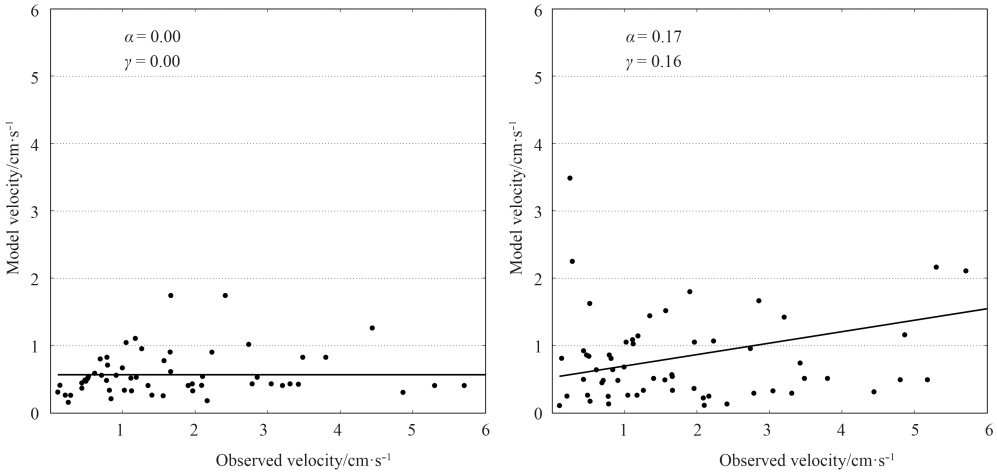

Fig. 2. Correlations of simulated velocity magnitudes with mooring current velocities for the WP (a) and the EF (b), respectively. α is the slope of regression line, and γ represents the correlation coefficient, respectively.

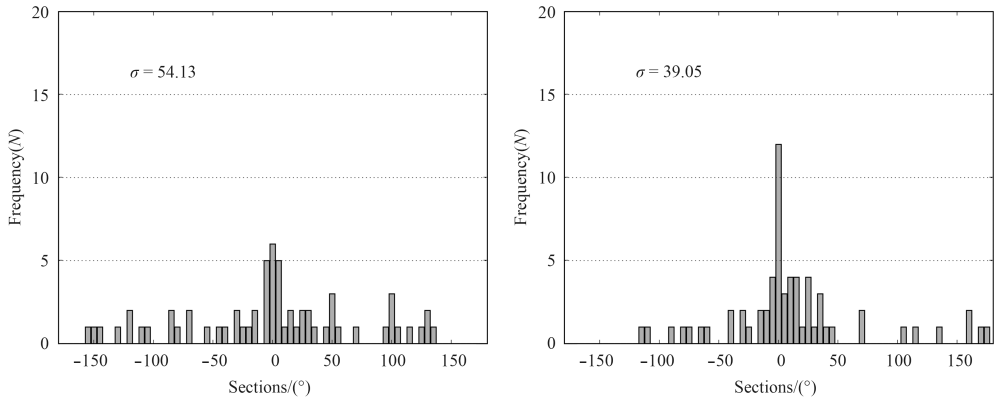

Fig. 3. Distributions of differences in current direction between simulated results and mooring current velocities. a. Results from the WP case and b. from the EF. σ indicates the average of difference values.

In all cases with parameterizations, correlations of the velocities become dramatically higher, compared to the WP correlations. In addition, both the magnitude and the differences in current direction are much better in the WP and the cases with parameterization than those using the EF model results.

3.3 *Comparison between the observations and model results*

Comparisons between the moored current meter velocities and the model current velocities are shown in Fig. 10. The NE and GL cases show much better agreements with observed velocities compared to the WP. The IS site (40.61°N, 139.36°E), southwest of Hokkaido on a steep slope, shows quite good agreements between the model and observation results in the NE and GL cases. Also, both parameterized cases show almost exactly the same direction as the observations at the HU site (42.5°N, 139.17°E), west of Hokkaido. The vector correlation of Crosby et al. (1993) is adopted to determine the degree to which the moored current data and the model results correspond. The correlation coefficients are 0.60 (WP), 0.80 (NE), and 0.84 (GL) for the northern EJS, and 0.38 (WP), 0.43 (NE), and 0.43 (GL) for the southern EJS. Not surprisingly, the vector correlation results between the mooring observations and the parameterized simulations (NE and GL) are very similar to those between the mooring observations and the Array for Real-time Geostrophic Oceanography (Argo) float velocities (0.80 and 0.42 for the northern and southern EJS, respectively, in CY10).

For every case of the correlation analysis, the GL is superior to the other cases. In contrast, the NE case correlates poorly with the Argo float velocities, and the correlation in the northern EJS is even smaller than that in the southern EJS.

Given the good agreements of the parameterized model cases with the mooring observations, the model results are also compared with the Argo float displacement velocities in the areas where sufficient observational velocities are available. Vector correlation coefficients between the Argo float displacement velocities and the simulations are 0.40 (WP), 0.34 (NE), and 0.63 (GL) for the northern EJS, and 0.18 (WP), 0.36 (NE), and 0.42 (GL) for the southern EJS. The GL model results in the northern EJS yield the highest correlation.

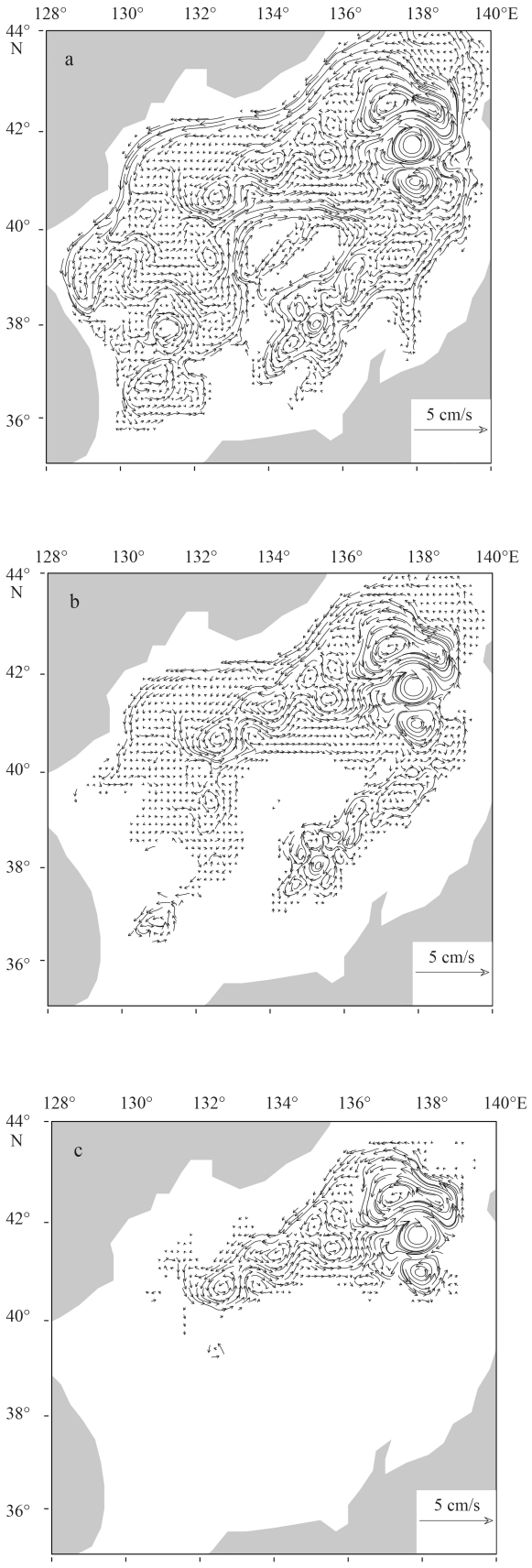

Fig. 4. Annual average of horizontal current velocity fields obtained from the EF at 1 000 m (a), 2 000 m (b), and 3 000 m (c) depth, respectively.

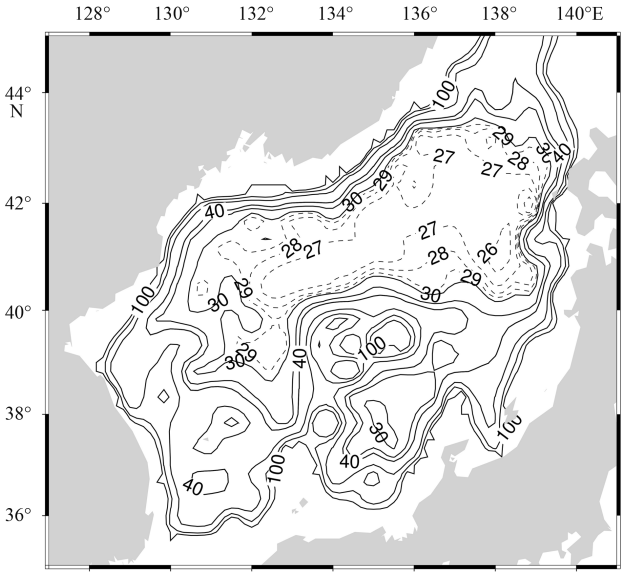

Fig. 5. Ambient potential vorticity (f/H) contours in the EJS. Solid lines indicate larger values than 30×10^9 m^{-1}·s^{-1}, with contour interval of 20×10^9 m^{-1}·s^{-1}. Dashed lines indicate smaller than 30×10^9 m^{-1}·s^{-1}, with contour interval of 1×10^9 m^{-1}·s^{-1}.

3.4 *Deep current fields in the numerical models*

The model current fields averaged over the deep layer from 800 m to the bottom for the WP, NE, GL cases and Argo displacement velocities are shown in Fig. 11. In the WP, the deep current velocities are no stronger than 2 cm/s, and the deep circulation pattern in the Japan Basin (hereafter JB) does not correspond well with the observed velocity field (Fig. 11d). The deep currents in the WP case are very weak, suggesting that neither surface wind stress nor thermohaline forcing, known to be a major driving force of the ocean circulation, drive the deep layers directly.

In the NE case, several significant features different from those in the WP are found. The NE deep current velocities are much stronger than those in the WP. Strong deep current flows follow along the steep slope regions in the three basins and agree well with observations. Strong southward currents along the east Korean coastal areas that then turn into the Ulleung/Tsushima Basin (hereafter UTB) are reproduced, which have also been observed (Senjyu et al., 2005; Teague et al., 2005) and simulated (Holloway et al., 1995). It should be noted that circulation in the southern basins (the UTB and Yamato Basin (hereafter YB)) are cyclonic in contrast with the WP results. These flow patterns persist over all seasons. Although the NE shows dramatic improvements in the deep current simulation, there are important features that still differ from the observational data. In the JB interior, especially in the region deeper than 3 000 m, neither the circulation pattern nor the velocity magnitude is in good agreement with observations. The NE model results show the maximum velocity magnitude to be only a few cm/s in the JB interior where are areas of mild topographic gradient.

In the GL case, the overall structure of the deep circulation is in good agreement with the observations (CY10; Danchenkov et al., 2003). Even in the JB interior, and especially in the region deeper than 3 000 m, the circulation pattern and the velocity

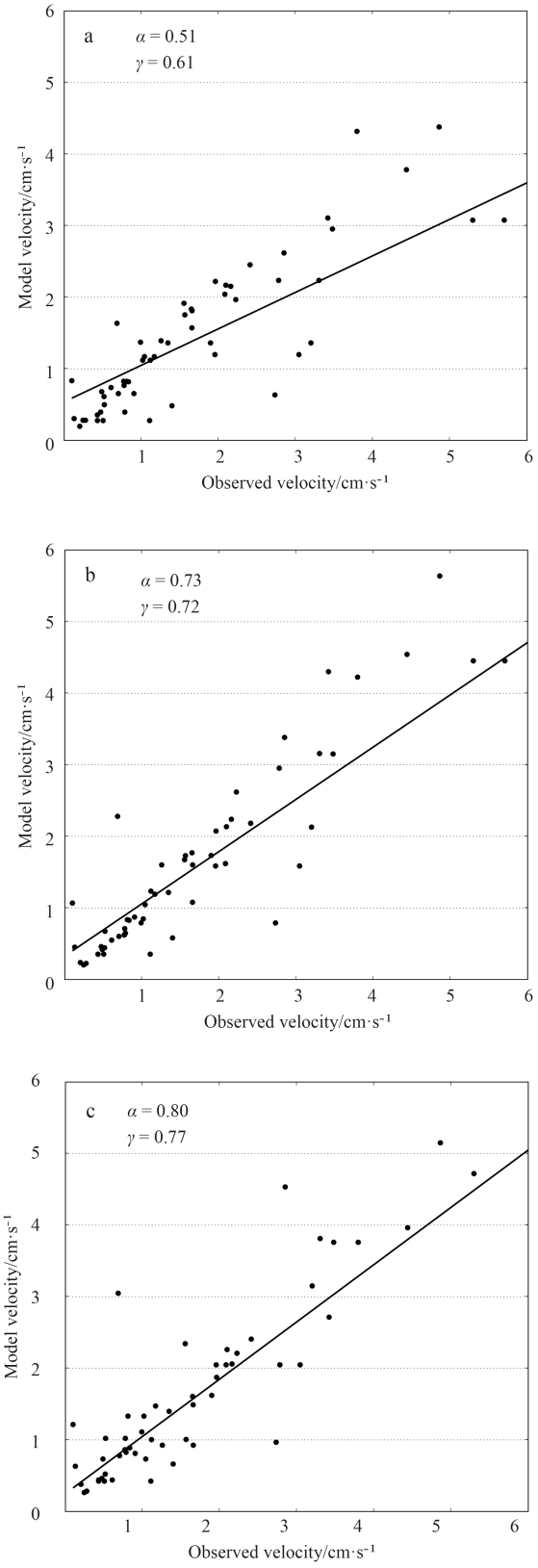

Fig. 6. Correlations of simulated velocity magnitudes with mooring current velocities for NE1 (a), NE2 (b), and NE3 (c) case, respectively. α is the slope of regression line, and γ represents the correlation coefficient, respectively.

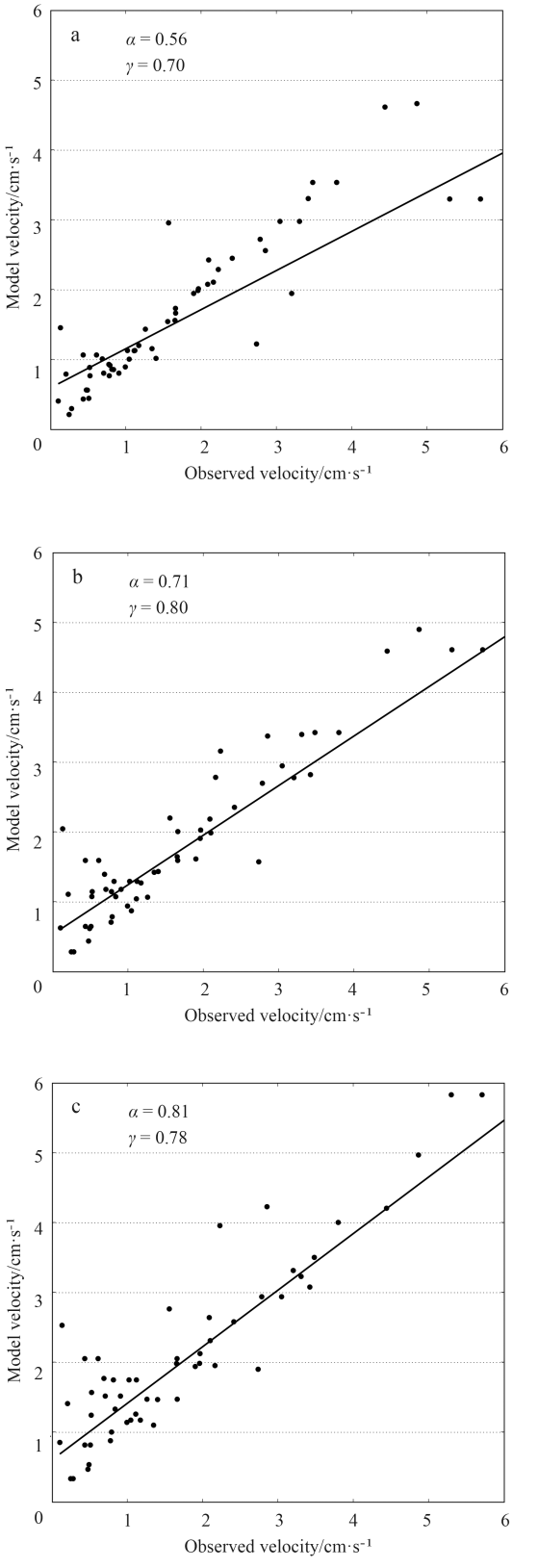

Fig. 7. Same as Fig. 6 except for GL1 (a), GL2 (b), and GL3 (c) case, respectively.

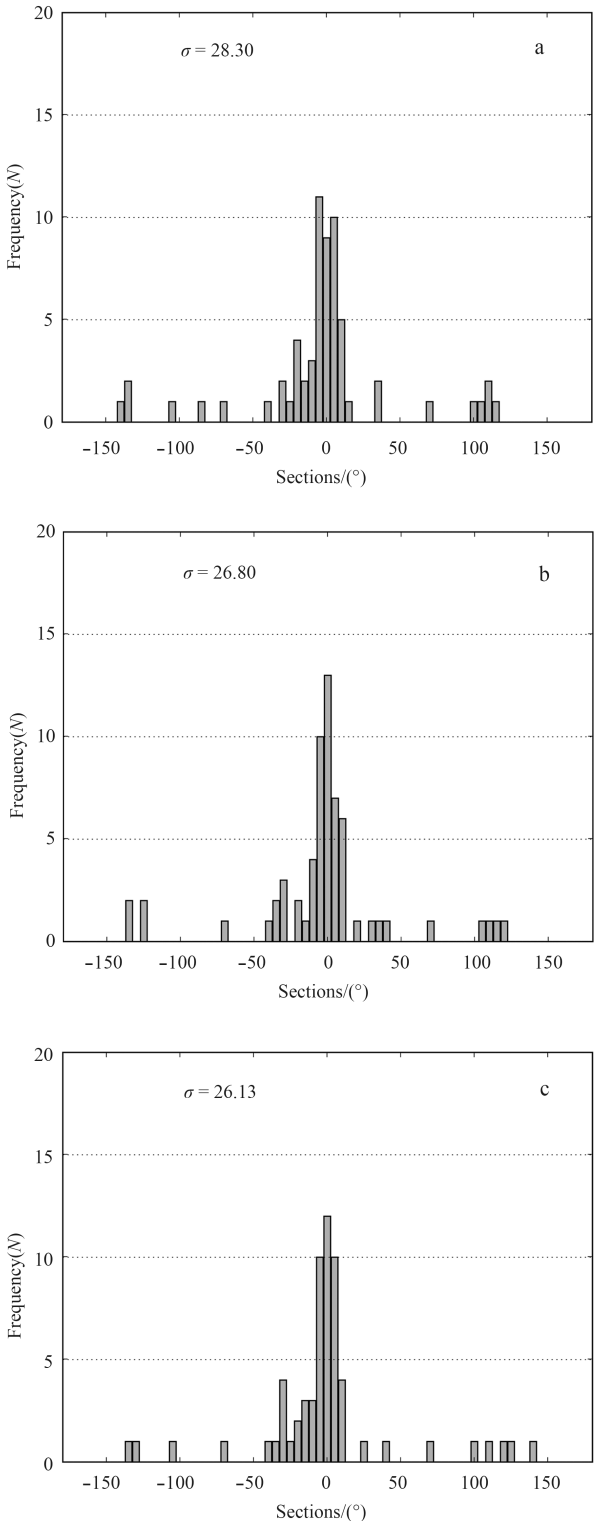

Fig. 8. Distributions of differences in current direction between mooring current velocities for NE1 (a), NE2 (b), and NE3 (c) case model velocities, respectively. σ indicates the average of difference values.

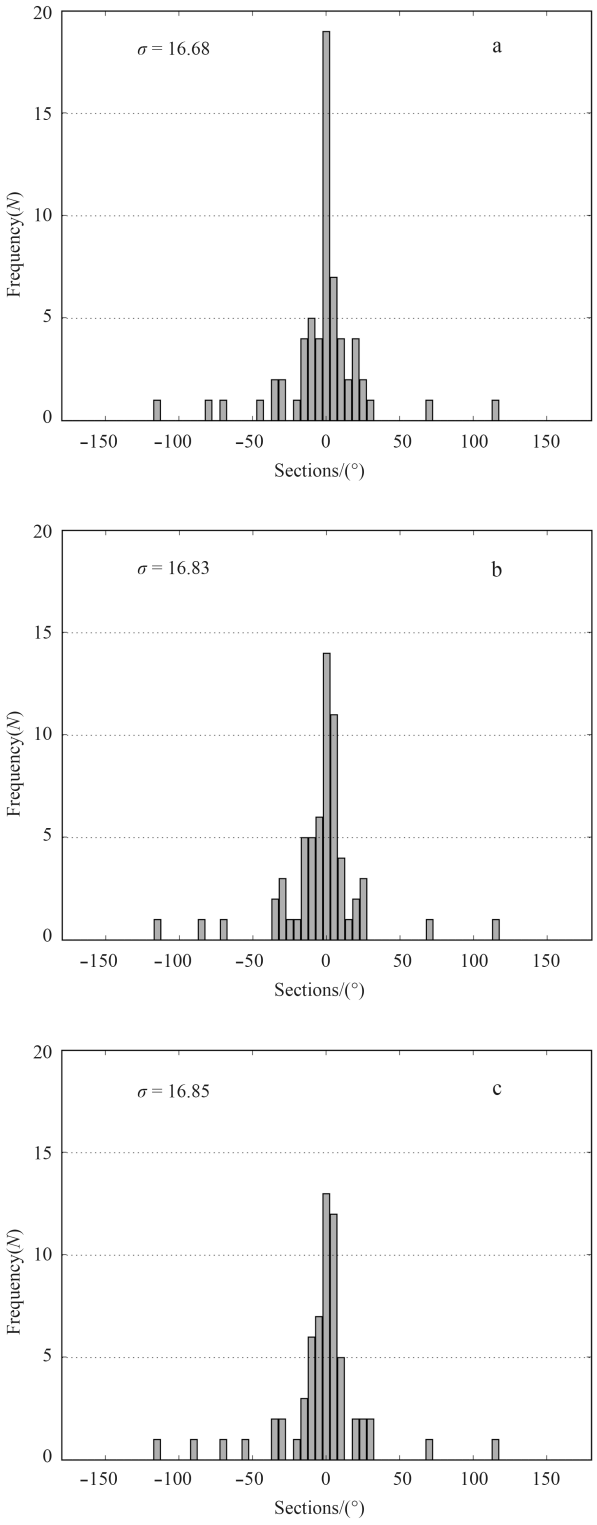

Fig. 9. Same as Fig. 8 except for GL1 (a), GL2 (b), and GL3 (c), respectively.

magnitude are in good agreement. GL model results show the currents in the JB interior to have strong velocity magnitudes (exceeding 6 cm/s) which are correspond with observed data (Fig. 11d).

3.5 *Volume transport*

Vertically averaged velocity fields from 800 m to bottom are inverted to obtain the geostrophic stream function in the EJS deep layer solving the Helmholtz equation as

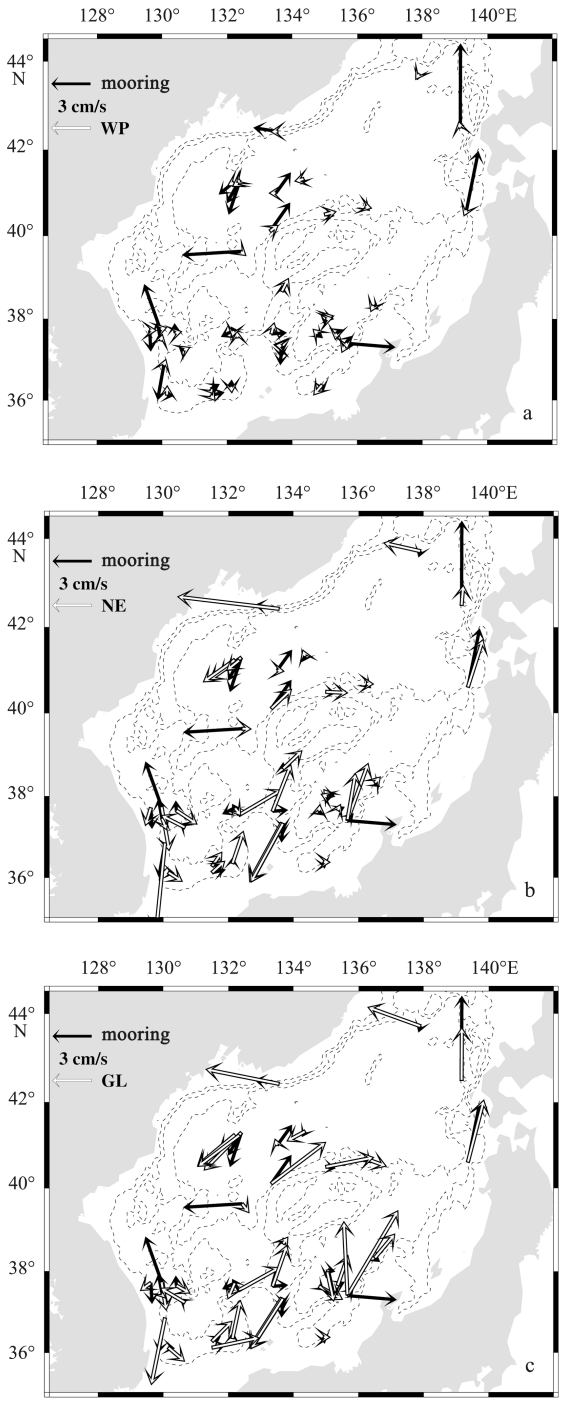

Fig. 10. Comparison between annually averaged mooring current velocities at each site (black arrows) and model results (outlined arrows) obtained from the WP (a), NE (b), and GL (c) case, respectively.

$$\nabla^2\psi = (hv)_x - (hu)_y, \tag{1}$$

where ψ is the stream function, h is the depth from 800 m to bottom, and (u,v) is the vertically averaged velocity from 800 m to bottom, respectively. Note that the deep layer from 800 m to bottom is approximated to be closed and non-divergent in vertical. Figures 12–15 show annual mean stream functions for Argo (provided by CY10), WP, NE, and GL, respectively. Although a basin wide cyclonic gyre in the JB, with the volume transport much larger than those in the southern basins, is a common feature in each case, significant differences among the cases are found in the structure and magnitude of the volume transport stream functions. The maximum transport in each case is 2.2×10^6 m^3/s in WP, 7.1×10^6 m^3/s in NE, and 10.1×10^6 m^3/s in GL. The maximum transport in the GL, which is approximately five times larger than that of the WP, agrees quite well with the observed transport of 10.2×10^6 m^3/s (Fig. 12). The position of maximum transport (core of the gyre) in the WP and NE cases is in the western JB, while that of the GL is located at around (41.5°N, 137.5°E), which is fairly close to the observed position (Fig. 12; 42°N, 138°E). It should be noted that the GL circulation pattern shown by the stream function in the JB is also in quite good agreement with the observed feature shown in Fig. 12.

The circulations in the UTB deep layer are cyclonic in both the NE and GL cases. In the GL case, the anti-cyclonic eddy field centered at (38°N, 131.2°E) is found around Ulleung Island. A corresponding anti-cyclonic eddy is found in the observational analysis (Fig. 12), although the transport volume of the anti-cyclonic eddy by the GL simulation is only approximately 40% of the observed volume (0.37×10^6 m^3/s for the GL and 0.97×10^6 m^3/s for the observational analysis). The anti-cyclonic eddy is very weak in the NE.

Teague et al. (2005) calculated 0.68×10^6 and 0.38×10^6 m^3/s as the inflow/outflow transports, respectively, integrated from 250 m to the bottom through the Ulleung Interplain Gap (UIG) from a (1/32)° NLOM model result. In the WP, no significant flow is seen in the UTB stream function (Fig. 13b). The flow structure in the UTB stream function in the NE case differs to a fair degree from that of the (1/32)° NLOM results, which suggest that the inflow to the UTB is mainly through the UIG and the outflow is divided into two routes—the western and eastern Dok Island channels (Teague et al., 2005). The major inflow to the UTB in the NE is the western channel of the Ulleung Island and the major outflow is through the UIG. The inflow and outflow through the UIG below 800 m (250 m) in the NE are 0.1×10^6 m^3/s (0.14×10^6 m^3/s) and 1.2×10^6 m^3/s (1.68×10^6 m^3/s), respectively, yielding a net outflow transport of 1.1×10^6 m^3/s (1.54×10^6 m^3/s). In the GL, inflow and outflow below 800 m (250 m) through the UIG are 0.7×10^6 m^3/s (0.98×10^6 m^3/s) and 1.1×10^6 m^3/s (1.54×10^6 m^3/s), respectively, showing a significant similarity in the inflow transport to that in the CY10 (0.7×10^6 m^3/s, below 800 m) and the inflow also reasonably correspond to Teague et al. (2005) (0.68×10^6 m^3/s, below 250 m). Moreover, the major inflow in the GL is through the UIG channel, agreeing well with the Argo analysis (Fig. 12) and with Teague et al. (2005). The large outflow through the UIG in the GL simulation seems to be due to the very small number of grids in the eastern channel of Dok Island.

The flow patterns in the UTB obtained by the two parameterization methods do not consistently correspond well with observed features. The simulated circulation is cyclonic throughout the year, while the flow field obtained from the analysis of observational data (Fig. 12) shows a more complex structure similar to that of Teague et al. (2005).

Both the NE and the GL cases show a basin-wide cyclonic circulation in the YB all year around, while the WP shows a basin-wide anti-cyclonic circulation in the YB. The maximum transport values in the YB are 2.1×10^6 m^3/s (NE) and 3.4×10^6 m^3/s (GL), while that for the WP is very small (< 0.4×10^6 m^3/s).

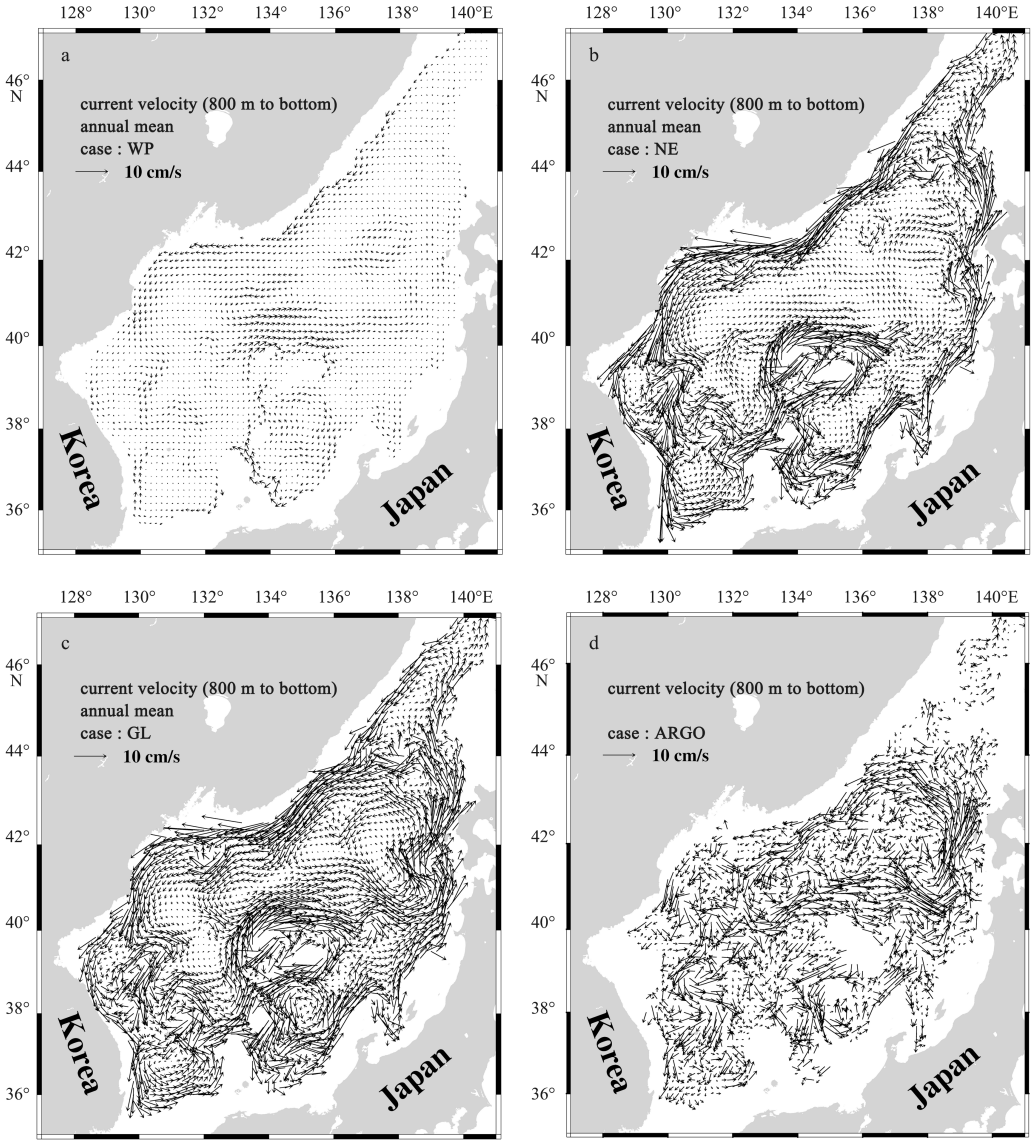

Fig. 11. Annual mean of velocity filed in the deep layer (800 m to bottom) for the WP (a), NE (b), GL (c) case, and regridded Argo displacements (d). Vectors are plotted every (1/6)°.

3.6 *Seasonal variation of deep circulation*

The monthly variations in the simulated maximum transport values are shown in Fig. 16. The GL shows a seasonal variation that strengthens in winter and weakens during summer to fall, which corresponds well to the seasonality of the observed velocities that intensified from late winter to early spring and weakened toward summer (CY10; Takematsu et al., 1999). The NE shows a seasonal variation similar to that of the GL, but the amplitude is weaker. The WP shows a weak seasonal variation compared with the other two, but with two maxima in May and November.

The seasonal variability of the monthly averaged velocity magnitudes in the EJS deep layer for the northern EJS (>40°N) and southern EJS (< 40°N) are shown in Fig. 17. The monthly and spatially averaged velocity is defined as follows:

$$\left|\vec{U}\right| = \frac{\int_0^x \int_0^y \int_z^0 \int_0^t \left|\vec{u}\,(x,y,z,t)\right| \mathrm{d}x\mathrm{d}y\mathrm{d}z\mathrm{d}t}{V \cdot T}, \tag{2}$$

where $\left|\vec{u}\,(x,y,z,t)\right|$ is the magnitude of the current velocity, V is the volume, and T is the month. The GL shows similar seasonal variability with that of observed maximum transports in the northern EJS, while the NE maximum transports scarcely change at all. This is easily understood considering that the NE parameterization of topostress does not change in time. For the southern EJS, no significant seasonal variations are found in any of the cases, which correspond with the observed transport changes.

Compared to the monthly average of the observational analyses, the GL case shows the most similar seasonal variations in both the northern and southern EJS. The annual means of the spatially averaged velocities in the GL are 2.25 and 2.11 cm/s for the northern and southern EJS, respectively, while those of the Argo floats (moored current meters) for the northern and southern EJS are 2.85 (3.22) and 2.22 (1.79) cm/s, respectively (CY10). Note that in the southern EJS, the GL and NE show similar velocity average values.

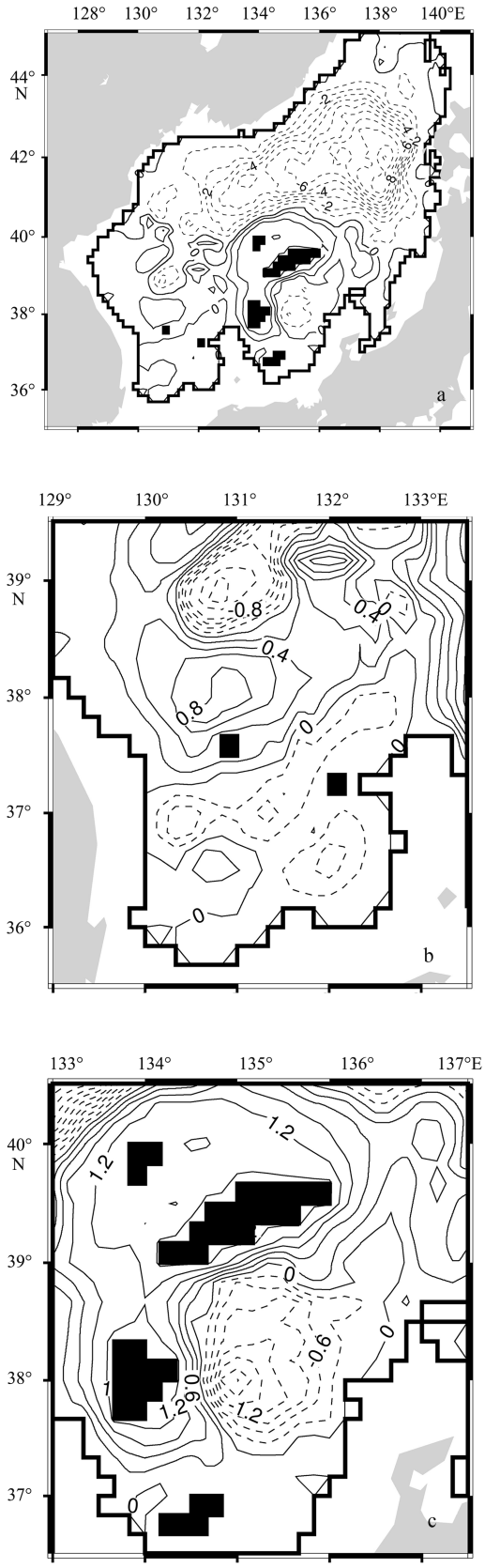

Fig. 12. Transport streamfunction from Argo float displacements for the EJS (contour interval is 1×10^6 m^3/s (<0) and 0.5×10^6 m^3/s (>0) (a), for the UTB (contour interval is 0.2×10^6 m^3/s) (b), and for the YB (contour interval is 0.3×10^6 m^3/s) (c), respectively.

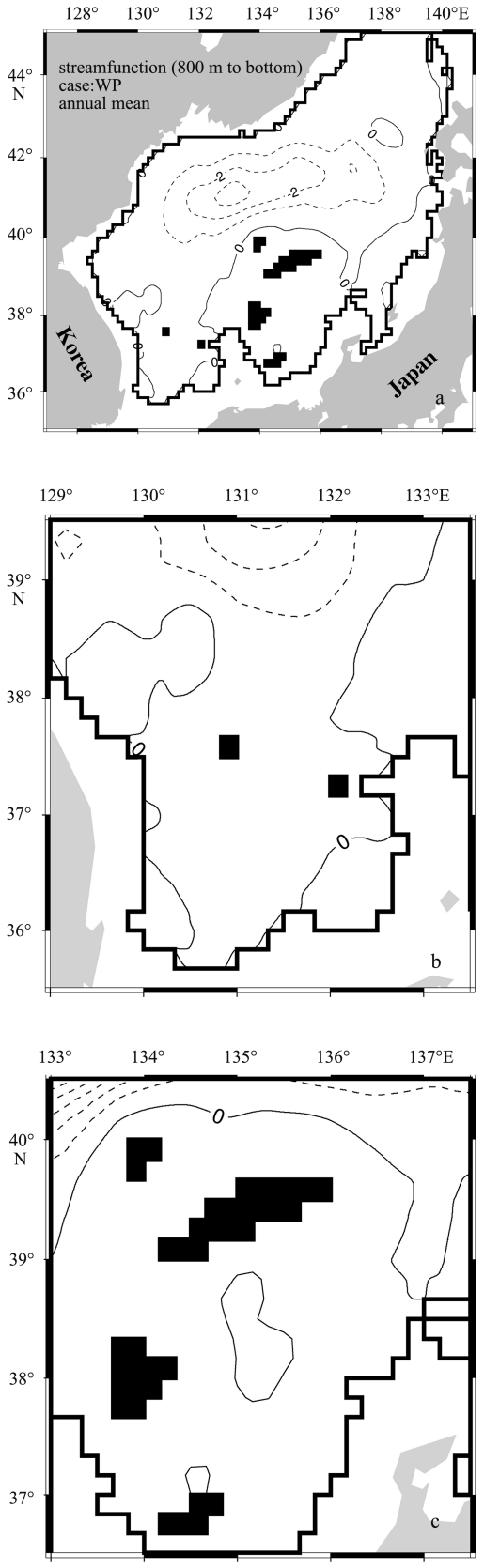

Fig. 13. Same as Fig. 12 except from the simulation results (WP).

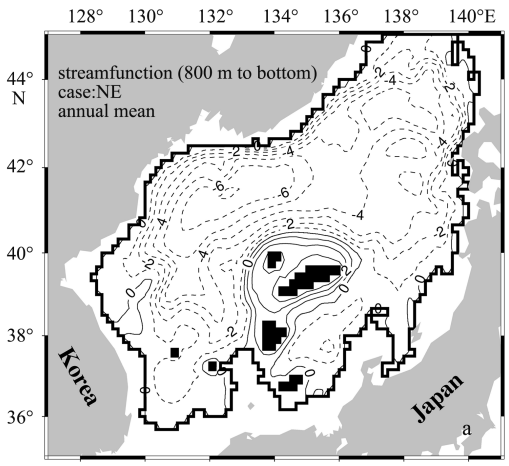

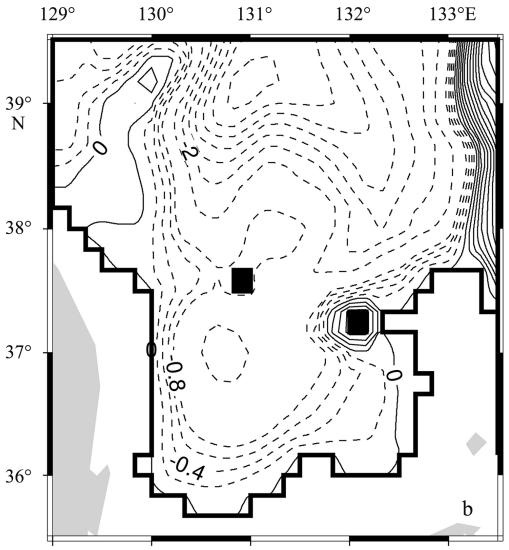

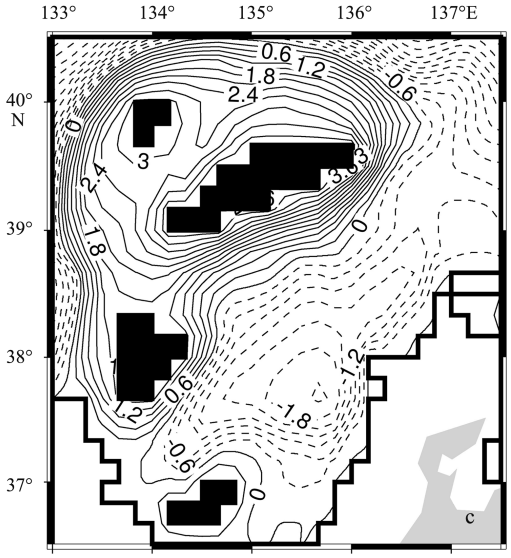

Fig. 14. Same as Fig. 12 except the NE.

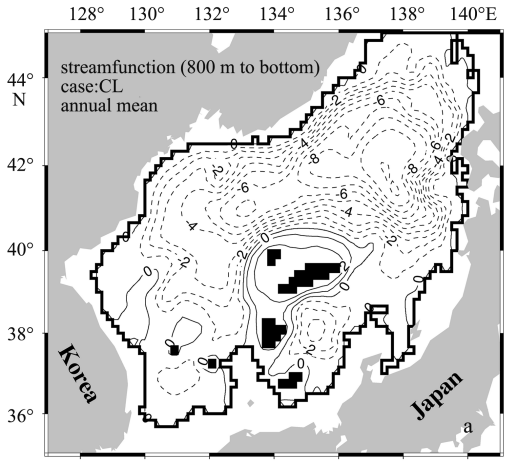

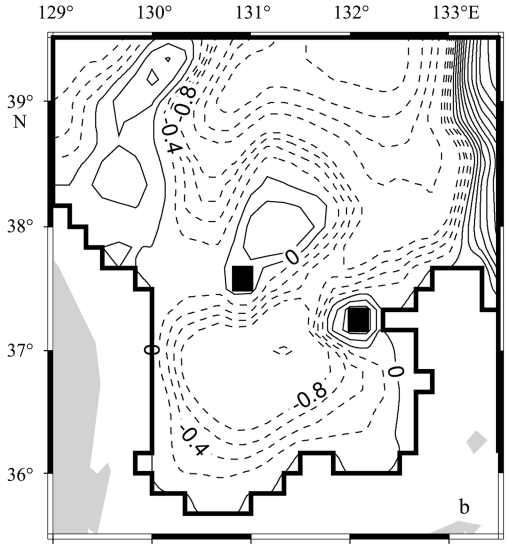

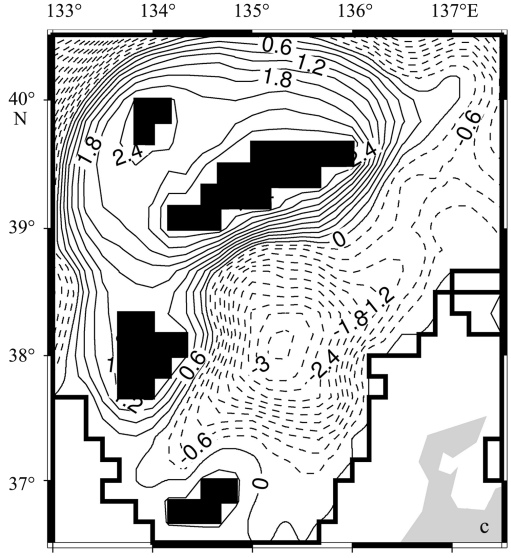

Fig. 15. Same as Fig. 12 except the GL.

3.7 *Topostrophy and surface current fields*

Topostrophy is a scalar index proposed by Merryfield and Scott (2007), and has been used to quantitatively estimate the topographic effect for flow (Maltrud and Holloway, 2008; Holloway,

2008; Holloway and Wang, 2009; Penduff et al., 2010). Topostrophy is defined as $\chi = \vec{f} \times \vec{u} \cdot \nabla H$, where $\vec{f}$ is the Coriolis vector, $\vec{u}$ is the velocity vector, and ∇H is the gradient of total depth.

From the definition, topostrophy is identified by the product of the Coriolis velocity and the slope of the topography. Therefore, the topostrophy will become larger when a current flows with its shallower regions to the right in the Northern Hemisphere. An upslope flow has zero topostrophy. In addition, the steeper the bottom slope, the larger the topostrophy. Following Holloway (2008), the topostrophy χ is normalized by $\sqrt{\left|f \times \vec{u}\right|^2 \left|\nabla H\right|^2}$ so that χ has a value between –1 and 1.

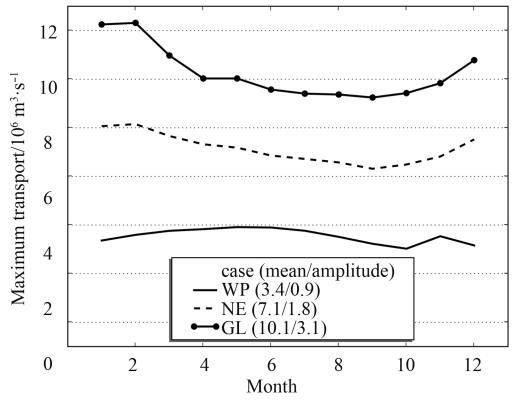

Fig. 16. Seasonal change of the maximum transport values for three simulation cases. Each line indicates the WP (solid), NE (dashed) and GL (circled), respectively. The descriptions in the legend indicate "the case name (annual average of maximum transport/annual amplitude)".

Figure 18 shows the topostrophy calculated from annually averaged velocity fields of the WP, NE, and GL cases. The topostrophy at each grid point is binned according to its depth and the bottom depth of the grid point. The horizontal and vertical axes indicate bottom depths and grid depths, respectively. For the WP case, the topostrophy χ is no larger than 0.9 for all regions and all depths. The largest value is shown around a bottom depth of 2 600 to 3 000 m where a relatively strong transport induced by wind stress is observed (Fig. 13). Note that in the EJS, only the JB has topography deeper than 2 500 m (Fig. 1). From both the observations (Holloway, 2008) and the numerical model results (Merryfield and Scott, 2007; Maltrud and Holloway, 2008), the topostrophy shows a bottom-intensifying tendency. However, topostrophy in the WP case shows smaller or even negative values near the bottom.

The NE case shows a clear tendency for topographic control and bottom intensification in the intermediate and deep layers. However, even in the surface and thermocline layers, the topostrophy shows very large values (>0.8), which indicates that the flow is mostly controlled by the ETI parameterization, ignoring other physical processes. In the regions where bottom depths are deeper than 3 000 m, equivalent to the JB interior, the topostrophy is much smaller than in other regions due to the weaker currents and smaller topographic gradients (Figs 11b and 14).

Overestimates of the ETI by the NE and GL simulations are shown in Fig. 19, which illustrates the surface current fields from the WP, NE, and GL cases. In the NE and GL simulations, a cyclonic flow along the surrounding coasts dominates the circulation in the EJS, and the East Korean Warm Current (EKWC) separates around the 36°N, while the WP simulation shows reasonable separation latitude (38°N). The NE shows the currents around the Yamato Rise (YR) running along the topography; however, in the GL, the currents do not strictly run along the topography of the YR.

4 Summary and discussion

Numerical model simulations with ETI parameterizations were successful in reproducing most of the observed features of the deep mean current in the EJS, which are expiscated in CY10. The results of our simulation study are summarized as follows.

(1) The ETI parameterizations (NE, GL) dramatically improved the model's performance in the deep layer, which successfully produced the cyclonic mean currents following the f/H contours. The EF model, which has an extra-fine grid scale and consumes a great amount of computational resources, shows weaker cyclonic currents than the ETI parameterization cases. Moreover, it shows an unusual anti-cyclonic eddy in the eastern JB.

(2) The velocities from both the profiling floats and the parameterized simulations are highly correlated with the moored current meter data (greater than 0.8). However, in the southern EJS, they showed poor vector correlation (approximately 0.4).

(3) The numerical simulations could not reproduce the detailed circulation structure of the UTB, described in CY10 and Teague et al. (2005).

(4) The GL simulation showed approximately 30% annual range of seasonal variability in the mean deep velocity in the JB, which agrees quite well with observational analysis. This suggests that the seasonal variability in the deep layer of the JB is strongly connected with eddy activities that interact with the bottom topography. The deep circulation in the UTB was not well reproduced in the GL case, however, suggesting that dynamics other than ETI may also play important roles in the UTB deep circulation.

The good agreement between the observed data and numerical model results detailed above tells us that the mesoscale eddies in the EJS play a major role in driving the deep mean currents in the EJS. Since the EJS has been described as a miniature world ocean (Kim and Yoon, 1996; Kim et al., 2001), successful simulations that include ETI parameterizations for the EJS deep layer can be applied in the global ocean in areas where mesoscale eddy activity is very high.

ETI results from an intrusion by the topography on the potential vorticity of the barotropic or quasi-barotropic flow. Thus, a higher potential vorticity gradient generates stronger deep mean currents (Hogan and Hurlburt, 2000; CY10). In the JB, the deep layer, below about 500 m, is occupied by the Japan Sea Proper Water (JSPW) and the vertical length of the JSPW uniform water mass is greater than 3 000 m. In the UTB, however, a strong surface current (EKWC) and the Ulleung Warm Eddy (UWE) vertically penetrate to depths below 250–300 m (Isoda and Saitoh, 1993; Shin et al., 2005), and consequently, the vertical scale of the quasi-barotropic layer is no greater than 1 500 m. Moreover, a cyclonic subpolar gyre over the JB flows in a similar direction with deep cyclonic circulation due to ETI, while the EKWC and UWE flow in an opposite direction to the ETI mean currents.

The JB interior has small topographic gradients, while those on the JB periphery are very large. CY10 suggested that the trans-

ports in the JB interior are as large as those around the JB periphery. The NE model results, which solely depend on the topographic gradient, show very small transports in the JB interior, whereas the GL gives similar results to those in CY10. In the deep layers, circulation can be controlled by small topographic changes. A barotropic or quasi-barotropic flow, impinging on an even small bathymetric change or obstacle, can be steered quasi-barotropically or induce a Taylor column. Transports by this phenomena are in proportion to the isopycnal thickness of the bottom water mass. For this reason, the EF, with (1/36)° resolution, cannot reproduce reasonable circulation in the JB interior because its z-coordinate vertical grid system does not conserve the isopycnal potential vorticity. Hogan and Hurlburt (2000), however, showed a strong circulation in the JB interior, similar to reported observations (Takematsu et al., 1999; Danchenkov et al., 2003; CY10), using a reduced-gravity model with coarser resolution (1/32°) than the EF. Therefore, the parameterizations based on a potential vorticity approach has advantages over z-coordinate simulations of ocean deep plains with small topographic variabilities.

The GL case also provides several advances compared with the NE case with respect to the topostrophy: First, large topostrophies are also observed in the JB interior, where bottom depth is greater than 2 800 m. Second, the effect of ETI is smaller than that in the NE case at the strongly stratified surface and thermocline layers. Rotating flows within the limits of area with weak or zero stratification have been investigated by many authors (Taylor, 1917; Huppert, 1975; Chapman and Haidvogel, 1992). When there is no stratification flow is independent of depth. In most geophysical flows the relative vorticity is far smaller than f, so the flow must follow the f/H, satisfying potential vorticity conservation. With stratification, the effect of topography drops off with height. The GL case is distinguished from the NE by the point that the GL generates the eddy-induced transport by isopycnal fluxes, thus the along-slope direction forcing by the form drag in the bottom layer fades off near the thermocline. The GL case shows bottom-intensifying large topostrophy in the regions deeper than 500 m where the bottom depth is greater than 1 000 m, and where the density structure is quasi-homogeneous (the JSPW). Although the GL shows better vertical structure results than the NE, both ETI parameterizations for the OGCM are vulnerable to disturbance of the ETI effects on the surface currents. Since topography is the only independent variable for the stream function, which the NE parameterization defines for the ETI, the ETI-generated flow affects whole water columns. Also, the GL parameterization overestimates the effect of the topographic gradient due to the mode-split time stepping method which calculates most of integration using the barotropic mode. Moreover, its variable vertical grids led to an overestimation of the bottom boundaries obtained from the topography gradient. Those factors cause a reduction in the western boundary currents and an inability to reproduce realistic circulation in the surface layers. A refinement of the vertical grids in the z-coordinate system might be a possible solution to this problem.

Although Takematsu et al. (1999) noted that the seasonal variation in the EJS deep layer is closely related to eddy variabilities, the NE case did not show significant seasonal variability, while the GL case showed clear seasonality. One of the possible candidates responsible for generating this seasonal variation is surface forcing, that is, wind stress and thermohaline forcing, which have a seasonal variation similar to that of the deep mean current. However, wind stress itself cannot directly induce a strong mean current larger than a few cm/s in the deep layer, as shown in many numerical models, without sufficient resolution to resolve mesoscale eddies, e.g., Kim and Yoon (1996).

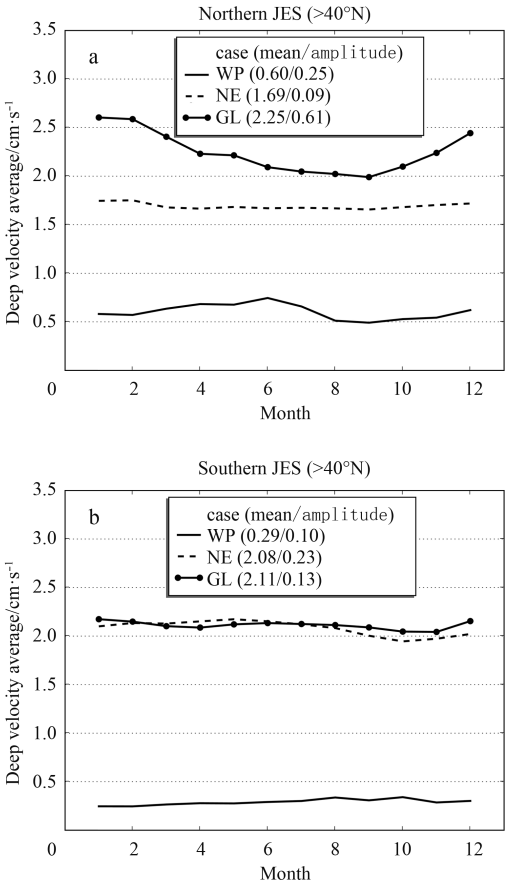

Fig. 17. Seasonal change of the velocity average in the northern (a) and southern (b) EJS for three simulation cases. Each line indicates the WP (solid), NE (dashed) and GL (circled), respectively. The descriptions in the legend indicate "the case name (annual average of maximum transport/annual amplitude)".

If wind stress energy is converted into mesoscale eddies through baroclinic instability as a result of the accumulation of available potential energy (APE), it might be able to generate a deep mean circulation. The process of how baroclinic eddies at the surface transfer energy to the deep layer has been studied by many authors (Dewar, 1998; Greatbatch, 1998; Greatbatch and Li, 2000; Hogan and Hurlburt, 2000). Hogan and Hurlburt (2000) showed the transfer of baroclinic eddy energy at the surface to the deep ocean, reproducing successfully the eddy-driven deep mean flow following the f/H contour in the Japan/East Sea using a primitive four layer model with extra fine horizontal resolution (<(1/32)°). One possible explanation for this mechanism, proposed by Dewar (1998), is that eddy-driven potential vorticity fluxes accelerate the deep currents following closed potential vorticity contours (f/H). Greatbatch (1998) and Greatbatch and Li (2000) proposed a similar mechanism for the generation of deep

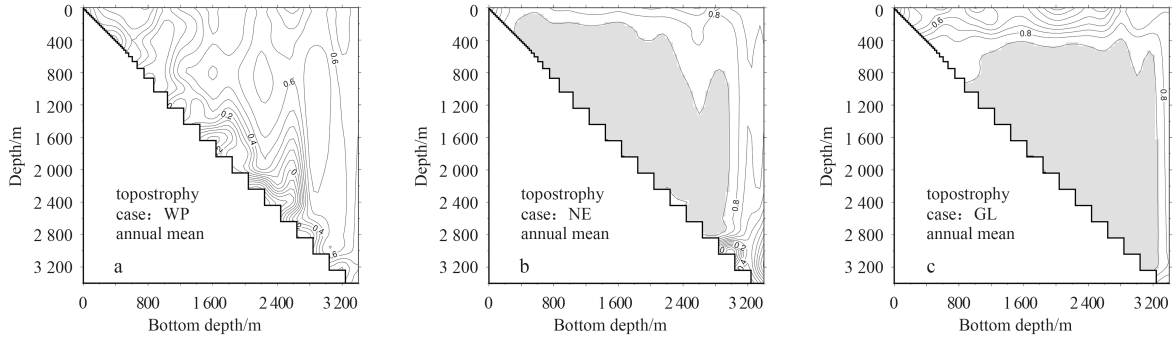

Fig. 18. Topostrophy from annually averaged velocity field for the WP (a), NE (b), and GL (c) cases, respectively. Contour interval is 0.05 and shaded section indicate the topostrophy is larger than 0.9.

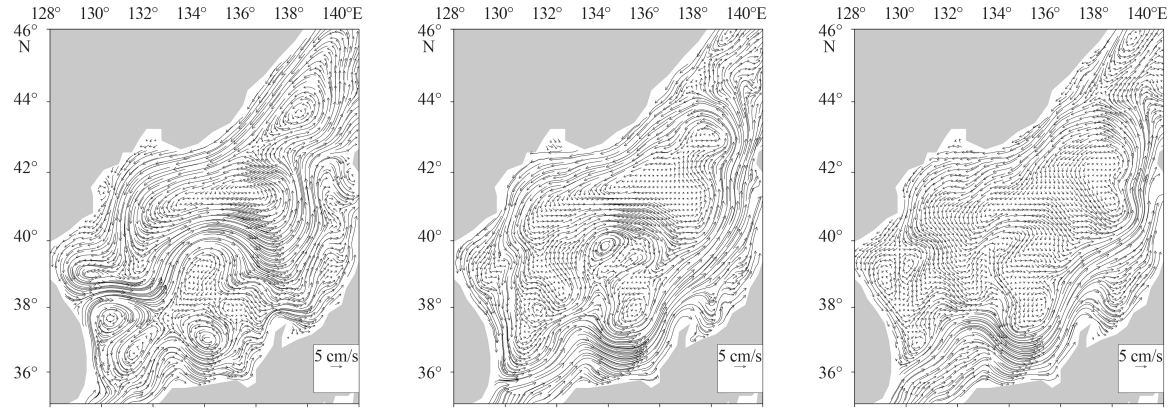

Fig. 19. Annual average of horizontal surface current velocity fields obtained from the WP (a), NE (b) and GL (c), respectively.

mean flow, but in contrast to Dewar (1998), focused on eddy-topography interaction.

Actually, the wind stress can act as a forcing to accumulate APE from late autumn to the end of winter. Cooling, as thermohaline forcing in the monsoon season, can also increase APE-inducing convection to an intermediate layer during typical winters in the EJS. The increased horizontal density gradient associated with the winter convection leads to the increase in APE. The APE then starts to decrease toward autumn mainly because of the conversion to kinetic energy due to baroclinic instability, resulting in the weakening of deep mean currents towards autumn until the monsoon starts again. To support the above hypothesis on the seasonal variation of the deep mean current from the viewpoint of APE, this study calculate the seasonal variation of the APE and the growth rate of baroclinic instability $(f/N)\mathrm{d}U/\mathrm{d}z$ (Charney, 1947; Eady, 1949) (Fig. 20) to know whether baroclinic eddy generation changes in a way similar to the surface forcing. Both the buoyancy frequency N and the vertical shear of zonal velocity $\mathrm{d}U/\mathrm{d}z$ are calculated over the depth of 300 m from the sea surface using the thermal wind relationship. The author also evaluated the seasonal variation of APE in the EJS, which is a source of energy for baroclinic instability. In a stratified ocean, APE is the difference between the total potential energy and that of a reference state, which is dynamically inactive. In this study, the APE is calculated following the notation of Oort et al. (1989) as

$$APE = -\frac{1}{2}g\int\frac{(\rho-\tilde{\rho})^2}{(\partial\tilde{\rho}_\theta/\partial z)}\mathrm{d}V, \tag{3}$$

where ρ is the local *in situ* density and $\tilde{\rho}$ is the horizontal average of *in situ* density at a local depth. Here, $\partial\tilde{\rho}_\theta/\partial z$ is the vertical stability of the horizontally averaged density expressed in terms of the change in potential density with depth. The temperature and salinity data for the calculation of the APE and growth rate of baroclinic instability are provided by Marine Information Research Center (MIRC) of the Japan Hydrographic Association (MIRC Ocean Dataset 2005).

Irregularly distributed temperature and salinity data are averaged and interpolated onto regularly spaced grids ((1/6)°×(1/6)°) by the nearest-neighborhood weighting (Wessel and Smith, 1998) with 1 degree search radius. The data period used is from 1971 to 2003. Figure 20 shows climatological monthly variations of APE and growth rate of baroclinic instability in the northern and southern EJS which are bounded by 40°N. Since the data in the northern EJS is generally sparse, the calculation in the northern EJS is conducted for the region (40°–46°N, 136°–139°E) which covers most of the eastern JB. The APE and growth rate in the northern EJS show the seasonal variations with a maximum in February and minimum in summer which are in good agreement with the seasonal change of the deep mean current. The APE in the southern EJS does not show significant seasonal variation, whereas the growth rate in the southern EJS show the similar seasonal variation to that of the mean current in the northern EJS, but the amplitude in winter is smaller than that in the northern EJS. These differences in seasonal changes of APE and growth rate between the northern and southern EJS might be a possible reason for the weak seasonal variability of deep mean current in the southern EJS as well as the geographical differences between the JB and other basins (UTB and YB) where horizontal extents are much smaller than the JB.

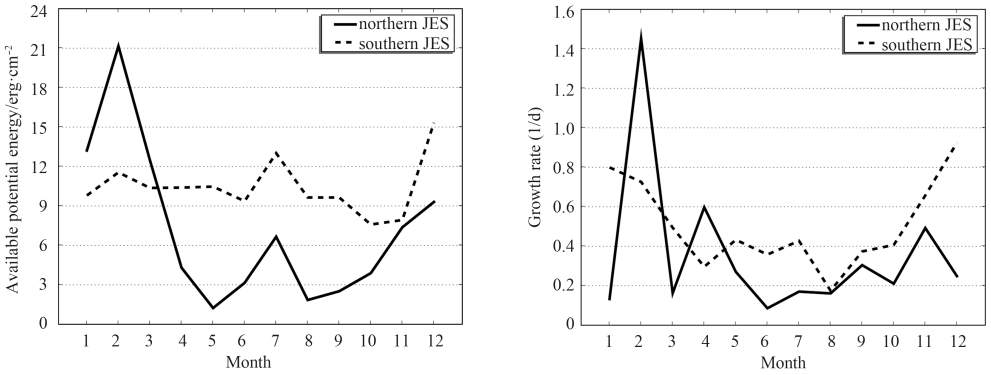

Fig. 20. Available potential energy (a) and $f/N(\mathrm{d}U/\mathrm{d}z)$ calculated from MIRC temperature and salinity data (b), respectively. Solid and dashed lines indicate the northern and southern EJS, respectively.

The GL parameterization adopts isopycnal gradients as a driving force in the surface and middle layers. Consequently the GL case is also available to reproduce the baroclinic driving mechanism of the deep mean circulation described above. The NE model, in contrast, is a function of depth and the time-independent function does not formulate seasonal variations induced by the baroclinic process. As a result, the GL case reproduces more realistic circulation in this study.

Acknowledgements

The author gratefully acknowledges the aid of Seung Y-H, in providing the idea that inspired this work. The advice and comments of Yoon J-H and Kida S are greatly appreciated. Comments by anonymous reviewers greatly helped improve the paper, and the author also wishes to thank Kim Y-J for providing her simulation data and paper. Riser S C, Korea Meteorological Agency, and Teague W J kindly provided PALACE observation data, APEX float trajectory data, and the current meter data, respectively.

References

Chapman D C, Haidvogel D B. 1992. Formation of Taylor caps over a tall isolated seamount in a stratified ocean. Geophysical & Astrophysical Fluid Dynamics, 64(1–4): 31–65

Charney J G. 1947. The dynamics of long waves in a baroclinic westerly current. J Meteor, 4(5): 136–162

Choi B H, Kim K O, Eum H M. 2002. Digital bathymetric and topographic data for neighboring seas of Korea. J Korean Soc Coastal Ocean Eng (in Korean), 14: 41–50

Choi Y J, Yoon J-H. 2010. Structure and seasonal variability of the deep mean circulation of the East Sea (Sea of Japan). J Oceanogr, 66(3): 349–361

Crosby D S, Breaker L C, Gemmill W H. 1993. A proposed definition for vector correlation in geophysics: theory and application. J Atmos Oceanic Technol, 10(3): 355–367

Danchenkov M A, Riser S C, Yoon J-H. 2003. Deep currents of the central Sea of Japan. Pacific Oceanogr, 1: 6–11

Dewar W K. 1998. Topography and barotropic transport control by bottom friction. J Mar Res, 56: 295–328

Eady E T. 1949. Long waves and cyclone waves. Tellus, 1(3): 33–52

Eby M, Holloway G. 1994. Grid transformation for incorporating the Arctic in a global ocean model. Climate Dyn, 10(4–5): 241–247

Gent P R, McWilliams J C. 1990. Isopycnal mixing in ocean circulation models. J Phys Oceanogr, 20(1): 150–155

Greatbatch R J. 1998. Exploring the relationship between eddy-induced transport velocity, vertical momentum transfer, and the isopycnal flux of potential vorticity. J Phys Oceanogr, 28(3): 422–432

Greatbatch R J, Li Guoqing. 2000. Alongslope mean flow and an associated upslope bolus flux of tracer in a parameterization of mesoscale turbulence. Deep-Sea Res Pt I, 47(4): 709–735

Hanawa K, Mitsudera M. 1985. About constructing of daily mean values of ocean data. Coastal Res Note, 23: 79–87

Hirose N, Kawamura H, Lee H J, et al. 2007. Sequential forecasting of the surface and subsurface conditions in the Japan Sea. J Oceanogr, 63(3): 467–481

Hogan P J, Hurlburt H E. 2000. Impact of upper ocean-topographical coupling and isopycnal outcropping in Japan/East Sea models with 1/8° to 1/64° resolution. J Phys Oceanogr, 30(10): 2535–2561

Holloway G. 1992. Representing topographic stress for large-scale ocean models. J Phys Oceanogr, 22(9): 1033–1046

Holloway G. 2008. Observing global ocean topostrophy. J Geophys Res, 113(C7): C07054, doi: 10.1029/2007JC004635

Holloway G, Sou T, Eby M. 1995. Dynamics of circulation of the Japan Sea. J Mar Res, 53(4): 539–569

Holloway G, Wang Zeliang. 2009. Representing eddy stress in an Arctic Ocean model. J Geophys Res, 114: C06020, doi: 10.1029/2008JC005169

Huppert H E. 1975. Some remarks on the initiation of inertial Taylor columns. J Fluid Mech, 67: 397–412

Ishizaki H, Motoi T. 1999. Reevaluation of the Takano-Oonishi scheme for momentum advection on bottom relief in ocean models. J Atmos Oceanic Technol, 16(12): 1994–2010

Isoda Y, Saitoh S I. 1993. The northward intruding eddy along the East coast of Korea. J Oceanogr, 49(4): 443–458

Kim Y J. 2007. A study on the Japan/East Sea oceanic circulation using an extra-fine resolution model [dissertation]. Fukuoka: Kyushu University

Kim K, Kim K-R, Kim D-H, et al. 2001. Warming and structural changes in the East (Japan) Sea: A clue to future changes in global oceans? Geophys Res Let, 28(17): 3293–3296

Kim C H, Yoon J-H. 1996. Modeling of the wind-driven circulation in the Japan Sea using a reduced gravity model. J Oceanogr, 52(3): 359–373

Kitani K. 1987. Direct current measurement of the Japan Sea Proper Water (in Japanese). Nihonkai-ku Suisan Shiken Kenkyuu Renraku News, Japan Sea National Fisheries Research Institute, 341: 1–6

Lee H J, Yoon J-H, Kawamura H, et al. 2003. Comparison of RIAMOM and MOM in modeling the East Sea/Japan Sea circulation. Ocean and Polar Research, 25(3): 287–302

Luchin V A, Manko A N, Mosyagina S Y, et al. 2003. Hydrography of water masses (in Russian). In: Terziev F S, ed. Hydrometeorology and Hydrochemistory of Seas. Sankt-Petersburg: Hydrometeoizdat, 8: 157–256

Maltrud M, Holloway G. 2008. Implementing biharmonic neptune in a global eddying ocean model. Ocean Modelling, 21(1–2): 22–34

Merryfield W, Scott R. 2007. Bathymetric influence on mean currents in two high-resolution near-global ocean models. Ocean Modelling, 16(1–2): 76–94

Mesinger F, Arakawa A. 1976. Numerical methods used in atmospheric models, Volume 1. WMO/ICSU Joint Organizing Committee, GARP Publication Series No. 17

Minobe S, Sako A, Nakamura M. 2004. Interannual to interdecadal variability in the Japan sea based on a new gridded upper water temperature dataset. J Phys Oceanogr, 34(11): 2382–2397

Mori K, Matsuno T, Senjyu T. 2005. Seasonal/spatial variations of the near-inertial oscillations in the deep water of the Japan Sea. J Oceanogr, 61(4): 761–773

NCAR. 1989. NCAR ASCII Version of ETOPO5 earth surface elevation. Data Support Section, NCAR

Noh Y. 1996. Dynamics of diurnal thermocline formation in the oceanic mixed layer. J Phys Oceanogr, 26(10): 2183–2195

Oort A H, Ascher S C, Levitus S, et al. 1989. New estimates of the available potential energy in the World Ocean. J Geophys Res, 94(C3): 3187–3200

Penduff T, Juza M, Brodeau L, et al. 2010. Impact of global ocean model resolution on sea-level variability with emphasis on interannual time scales. Ocean Sci, 6: 269–284

Sakai R, Yoshikawa Y. 2005. Numerical experiments on the formation mechanism of abyssal current in the Japan Sea. Engineer Sci Rep Kyushu Univ (in Japanese), 26(4): 423–430

Salmon R, Holloway G, Hendershott M C. 1976. The equilibrium statistical mechanics of simple quasi-geostrophic models. J Fluid Mech, 75(4): 691–703

Senjyu T, Shin H R, Yoon J-H, et al. 2005. Deep flow field in the Japan/East Sea as deduced from direct current measurements. Deep-Sea Res Pt II, 52(11–13): 1726–1741

Senjyu T, Sudo H. 1996. Interannual variation of the upper portion of the japan sea proper water and its probable cause. J Oceanogr, 52(1): 27–42

Seung Y-H, Yoon J-H. 1995. Robust diagnostic modeling of the Japan sea circulation. J Oceanogr, 51(4): 421–440

Shin H R, Shin C W, Kim C, et al. 2005. Movement and structural variation of warm eddy WE92 for three years in the Western East/Japan Sea. Deep-Sea Res Pt II, 52(11–13): 1742–1762

Takano K. 1974. A General Circulation Model For the World Ocean. Numerical Simulation of Weather and Climate Technical Report. Los Angeles: Univ of California, 47

Takematsu M, Nagano Z, Ostrovski A, et al. 1999. Direct measurements of deep currents in the northern Japan Sea. J Oceanogr, 55(2): 207–216

Takikawa T, Yoon J-H. 2005. Volume transport through the Tsushima straits estimated from sea level difference. J Oceanogr, 61(4): 699–708

Taylor G I. 1917. Motion of solids in fluids when the motion is not irrotational. Proc Roy Soc, A93: 99–113

Teague W J, Tracey K L, Watts D R, et al. 2005. Observed deep circulation in the Ulleung Basin. Deep-Sea Res Pt II, 52(11–13): 1802–1826

Wallcraft A J, Kara A B, Hurlburt H E. 2005. Convergence of Laplacian diffusion versus resolution of an ocean model. Geophys Res Lett, 32(7), doi: 10.1029/2005GL022514

Webb D J, de Cuevas S J, Richmond C S. 1998. Improved advection schemes for ocean models. J Atmos Oceanic Technol, 15(5): 1171–1187

Wessel P, Smith W H F. 1998. New, improved version of generic mapping tools released. EOS Trans AGU, 79: 579

Yoon J-H, Kawamura H. 2002. The formation and circulation of the intermediate water in the Japan Sea. J Oceanogr, 58(1): 197–211

Appendix:

Here, the author introduces the parameterization of the eddy stress following GL. For convenience, Greatbatch (1998) assumed the momentum equations reduce to the geostrophic balance

$$-f\bar{v} = -\frac{1}{\rho_0}\frac{\partial \bar{p}}{\partial x}, \tag{A1}$$

$$f\bar{u} = -\frac{1}{\rho_0}\frac{\partial \bar{p}}{\partial y}, \tag{A2}$$

where p is the pressure, over-bar denotes averaged values, and ρ_0 is representative density for seawater.

These equations can be rewritten in terms of the tracer transport velocity

$$(U, V, W) = (\bar{u} + u_I, \bar{v} + v_I, \bar{w} + w_I). \tag{A3}$$

Then Eqs (A1) and (A2) yields

$$-fV = -\frac{1}{\rho_0}\frac{\partial \bar{p}}{\partial x} - fv_I, \tag{A4}$$

$$fU = -\frac{1}{\rho_0}\frac{\partial \bar{p}}{\partial y} - fu_I. \tag{A5}$$

Greatbatch (1998) assumes that the eddy-induced transport velocities $u_{\rm I}, v_{\rm I}$ appear as Ekman velocities given by

$$-fv_{\rm I} = \frac{1}{\rho_0}\frac{\partial X}{\partial z}, fu_{\rm I} = \frac{1}{\rho_0}\frac{\partial Y}{\partial z}. \tag{A6}$$

In the vector form, the eddy-induced transport velocity is expressed as

$$\boldsymbol{u}_{\rm I} = -\frac{1}{f\rho_0}\boldsymbol{k}\times\frac{\partial}{\partial z}(X, Y). \tag{A7}$$

Then,

$$-fV = -\frac{1}{\rho_0}\frac{\partial \bar{p}}{\partial x} + \frac{1}{\rho_0}\frac{\partial X}{\partial z}, \tag{A8}$$

$$fU = -\frac{1}{\rho_0}\frac{\partial \bar{p}}{\partial y} + \frac{1}{\rho_0}\frac{\partial Y}{\partial z}. \tag{A9}$$

The vector (X,Y) appears as a horizontally directed stress acting on the fluid. Greatbatch (1998) refers to (X, Y) as the eddy stress which is equivalent with the form drag.

$$(X, Y) = \overline{p'\nabla_\rho Z'}. \tag{A10}$$

Then Eq. (A7) can be written as

$$u_{\rm I} = -\frac{1}{f\rho_0}k\times\frac{\partial}{\partial z}\left(\overline{p'\nabla_\rho Z'}\right). \tag{A11}$$

Following the parameterization by GM90, the eddy stress (X,Y) is expressed as

$$(X, Y) = -\rho_0 f\kappa k\times\Gamma, \tag{A12}$$

where κ is the thickness diffusivity, k is a unit vector in the upward direction, and

$$\Gamma = -\frac{\nabla\bar{p}}{\bar{p}_z} = (R, S). \tag{A13}$$

The isopycnal slope $(R,S) = -\nabla_h\rho/\rho_{\bar{z}}$ is given in isopycnal coordinate by $(R,S) = \nabla_\rho\bar{Z}$. (X,Y) can be rewritten by a geostrophic velocity $\bar{\boldsymbol{u}}_g$ as

$$(X, Y) = \frac{\rho_0 f^2}{N^2}\kappa\bar{\boldsymbol{u}}_{gz}, \tag{A14}$$

where N is the local value of the buoyancy frequency. Equation (A14) shows that the eddy stress is parameterized by the vertical mixing of momentum with a coefficient of $\kappa f^2/N^2$.

Using Eqs (A12) and (A13), Eq. (A7) can be written as

$$\boldsymbol{u}_{\rm I} = -\kappa\Gamma_z = -\kappa(R, S)_z. \tag{A15}$$

Then Eqs (A7) and (A8) can be written as

$$-fV = -\frac{1}{\rho_0}\frac{\partial \bar{p}}{\partial x} + \kappa f\frac{\partial}{\partial\bar{z}}\{S\}, \tag{A16}$$

$$fU = -\frac{1}{\rho_0}\frac{\partial \bar{p}}{\partial y} - \kappa f\frac{\partial}{\partial\bar{z}}\{R\}, \tag{A17}$$

and in a vector form

$$f\boldsymbol{k}\times\boldsymbol{V} = -\rho_0^{-1}\nabla_h\bar{p} - \kappa f\boldsymbol{k}\times(R, S)_{\bar{z}}, \tag{A18}$$

where $\boldsymbol{V}$=(U,V). In conducting numerical experiments, the second term in Eq. (A18) is just added to the right hand side of Eq. (A1).

As for the equation of tracers, no parameterizations are incorporated to illuminate the effects of the eddy stress on the deep mean flow through the momentum transfer.

For the boundary conditions, (R, S) are set to be zero at the ocean surface and are identical to the gradient of the topography $(-\nabla H)$ at the bottom boundaries.

Regarding the equation for the tracers, no parameterizations are incorporated to illuminate the effects of eddy stress on the deep mean flow through the momentum transfer.